

RESEARCH

Open Access



# The human immune cell simulated anti-breast cancer nanorobot: the efficient, traceable, and dirigible anticancer bio-bot

Seyed Mohammad Reza Seyedi<sup>1</sup>, Ahmad Asoodeh<sup>1\*</sup> and Majid Darroudi<sup>2</sup>

\*Correspondence:  
Asoodeh@um.ac.ir

<sup>1</sup> Department of Chemistry,  
Faculty of Science, Ferdowsi  
University of Mashhad, Mashhad,  
Iran

<sup>2</sup> Department of Medical  
Biotechnology,  
School of Nanotechnology,  
School of Medicine, Mashhad University  
of Medical Sciences, Mashhad,  
Iran

## Abstract

**Background:** Various types of cancer therapy strategies have been investigated and successfully applied so far. There are a few modern strategies for improving drug selectivity and biocompatibility, such as nanoparticle-based drug delivery systems. Herein, we designed the traceable enzyme-conjugated magnetic nanoparticles to target human breast cancer cells by simulating the innate immune cell's respiratory explosion response.

**Methods:** The human immune cell simulated anti-breast cancer-nanorobot (hisABC-NB) was produced by conjugating the mouse-derived iNOS and human-originated MPO enzymes on the folate-linked chitosan-coated Fe<sub>3</sub>O<sub>4</sub> nanoparticles. The synthesized nanoparticles were functionalized with folic acid as the breast cancer cell detector. Then, the hisABC-NB's stability and structural properties were characterized by studying Zeta-potential, XRD, FTIR, VSM, FESEM, and DLS analysis. Next, the selectivity and anti-tumor activity of the hisABC-NB were comparatively analyzed on both normal (MCF-10) and cancerous (MCF-7) human breast cells by analyzing the cells' survival, apoptotic gene expression profile (P53, BAX, BCL2), and flow cytometry data. Finally, the hisABC-NB's traceability was detected by T2-weighted MRI imaging on the balb-c breast tumor models.

**Results:** The hisABC-NB significantly reduced the MCF-7 human breast cancer cells by inducing apoptosis response and arresting the cell cycle at the G2/M phase compared with the normal cell type (MCF-10). Moreover, the hisABC-NB exhibited a proper MRI contrast at the tumor region of treated mice compared with the non-treated type, which approved their appropriate MRI-mediated traceability.

**Conclusion:** The hisABC-NB's traceability, dirigibility, and selective cytotoxicity were approved, which are the three main required factors for an efficient anticancer compound. Therefore, it has the potential to be used as an intelligent safe anticancer agent for human breast cancer treatment. However, several in vitro and in vivo studies are required to clarify its selectivity, stability, and safety.

**Keywords:** Human immune cell simulated anti-breast cancer-nanorobot (hisABC-NB), MRI-mediated traceability, Selective cytotoxicity, Dirigibility, Apoptotic activity



## Background

Breast cancer (BC) represents approximately 23% of all women's cancer worldwide (Gupta et al. 2015). Iranian BC patients in 2015 reported 12,802 patients, which were almost (51%) under 50 years old. In time screening, detection, and preventive treatment are considered the main three-axis issues in reducing the global burden of all cancer types (Omidi et al. 2022). To find the most efficient targeted BC treatment strategy, it is required to have a deeper look at the tumor carcinogenesis process as well as the tumor-suppressive potentials of the human immune system.

The cancer progression requires continuous bioenergetics flow to respond to the cancer cell metabolic requirements (Kee and Cheong 2014) and anti-oxidative defense mechanisms for non-stop proliferation, even under stressful conditions (Arfin et al. 2021). It has been found that folate receptor- $\alpha$  (FLa) overexpression supplies the folate resources of cancer cells and grants their rapid proliferation (Cheung et al. 2016). Different areas in the body are prone to be transformed into primary cancer niches such as breast, ovarian, colorectal, and lung, which up-regulated the cell membrane FLa receptors (Norton et al. 2020). Therefore, FLa-tracing can detect FLa-expressing cancer cells, such as breast cancer, and can potentially be used as a traceable tumor marker detector by imaging techniques (Sega and Low 2008).

Cancer cells and other normal cells are vulnerable to reactive oxygen (ROS) and nitrogen (RNS) species such as hypochlorous acid and nitric oxide. In this regard, the first-line immune response to cancer cell proliferation is conducted by increasing the ROS/RNS nearby the cancer cells produced by white blood cells' innate immune response, such as M1 macrophages. They induce apoptosis-mediated cell cycle arrestment under ROS/RNS-induced inflammation conditions (Aboeella et al. 2021). In other words, M1 macrophages temporarily increase hypochlorous acid and nitric oxide levels nearby the cancer cells by secreting the local myeloperoxidase (MPO) (Ali et al. 2022) and inducible nitric oxide synthase (iNOS) (Singh and Gupta 2011) enzymes.

Various anticancer drugs have recently been investigated to induce cell-selective intracellular ROS-mediated apoptosis in cancer cells, which are mainly suggested to be used as nano-drug delivery systems (NDDS). The NDDSs are responsible for passively delivering the encapsulated anticancer compounds to the target cancer cell and inducing ROS-mediated apoptosis. Also, their biocompatibility and serum solubility make them more efficient (Jahan et al. 2021). In this regard, nanoparticles targeting breast cancer cell receptors such as EGFR- (Milane et al. 2011), Folate Receptor- (Alibolandi et al. 2016), and HER-2 (Kim et al. 2020) targeted drug-loaded NPs have been synthesized for the efficient delivery of anti-breast cancer compounds (Asadolahi et al. 2022).

In the current study, iNOS and MPO enzymes, the two potent inducers of the innate immune cell's respiratory explosion, have been immobilized on the individual folate-conjugated chitosan-coated  $\text{Fe}_3\text{O}_4$  nanoparticles to induce ROS/RNS-mediated apoptosis in MCF7 breast cancer cells. Therefore, the selectivity, toxicity, anticancer activity, and traceability of the magnetic traceable nano-carrier called human immune cell simulated anti-breast cancer-nanorobot (hisABC-NB) was studied on MCF7/MCF10 cell lines and murine breast cancer models (Fig. 1).

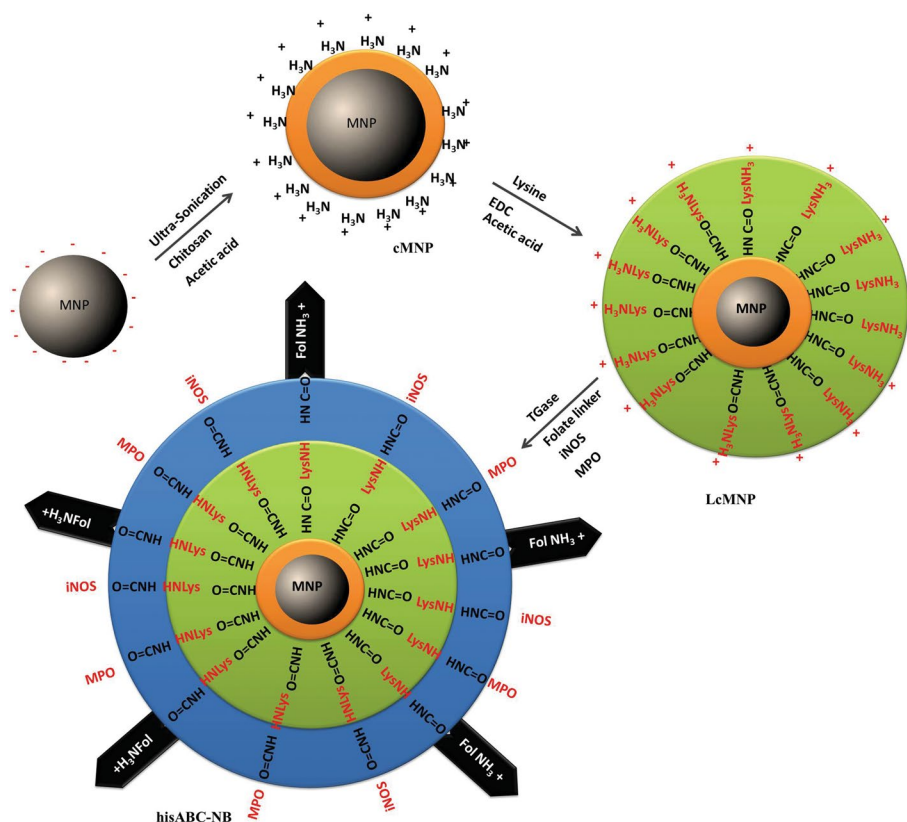


**Fig. 1** The hisABC-NB synthesis process. *MNP* magnetic nanoparticle, *EDC* 1-ethyl-3-(3-dimethylaminopropyl) carbodiimide, *iNOS* inducible nitric oxide synthase, *MPO* myeloperoxidase, *hisABC-NB* human immune simulated anti-breast cancer-nanorobot

## Results

### The hisABC-NB physicochemical characterization

The first-line characterization assays were utilized to evaluate the crystallinity, magnetism, morphology, size, and surface charge of the MNP nanoparticles by XRD, VSM, FESEM, DLS, and zeta potential techniques. The MNP’s size was determined at 19 nm by FESEM microscopy (Fig. 2Aa). Meanwhile, the DLS results exhibited a tenfold larger size for MNP particles at a Z-average of 212 nm. Regarding the mono-disperse production process of MNP (polydispersity index (PDI) value at 0.418) (Stetefeld et al. 2016), the results indicate the magnetism-based accumulation of MNP (Fig. 2Ab). The XRD pattern of MNP’s particle was detected by the six most common 2θ angles positions at 30.1°, 35.7°, 43.3°, 53.9°, 57.5°, and 63° (Fig. 2Ac).

The second line characterization analysis was continued by measuring the size and morphology of folate-linked coated lysine-chitosan MNP (FLcMNP). The TEM micrograph exhibits the spherical organized structure of FLcMNP at lower than 50 nm dimensions (Fig. 2B). The FESEM result showed a significant enlargement for FLcMNP nanoparticles at about 40 nm (Fig. 2Ca). The partial enhancement of PDI (0.448) does not change the mono-disperse processing condition. Therefore, the increased particle size (Fig. 2Cb) directly depends on the FLcMNP’s magnetism property. Moreover, the XRD pattern of the FLcMNP verifies its F<sub>3</sub>O<sub>4</sub> core and coating

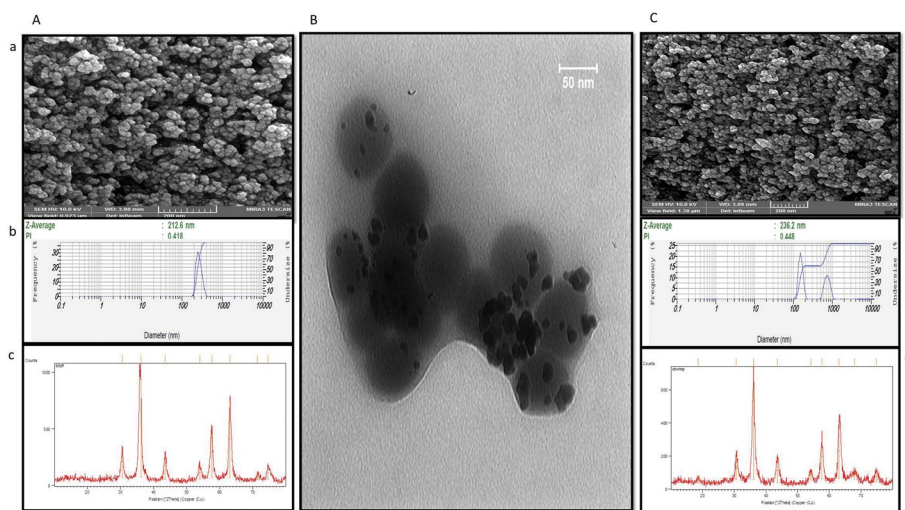


**Fig. 2** The MNP and FLCMNP characterization. The **A** and **C** columns show the MNP and FLCMNP nanoparticles' characterization. Part **B** shows the TEM micrograph of FLCMNP. **a** FESEM micrograph of the MNP (left) and FLCMNP (right) nanoparticles; **b** DLS results of the MNP (left) and FLCMNP (right) nanoparticles; **c**: XRD patterns of both the MNP (left) and FLCMNP (right); *MNP* magnetic nanoparticle, *FLCMNP* FOLATE-linked lysine-chitosan MNP

alterations by detecting the same  $2\theta$  angles sites and decreased peak intensity, respectively (Fig. 2Cc).

The magnetism activity and surface charge were analyzed for MNP and hisABC-NB. The results revealed a notable decreasing magnetism activity and remarkable enhancement of surface charge in hisABC-NB compared with MNP nanoparticles from 21.1 to 44.9 mV (Fig. 3).

The last line characterization process of the hisABC-NB was completed by verifying its chemical structure during production. The chitosan-coated MNP (cMNP) formation was confirmed by the appearance of typical characteristic absorption bands of chitosan-coated magnetic nanoparticles at 3407, 2925, 1626, and 1098  $\text{cm}^{-1}$  wavenumbers (Fig. 4A) (Pineda et al. 2014). The wavenumbers exhibited the chitosan structural atomic bonds, which are mentioned in Table 1.

As shown in Fig. 4B, the success in producing the lysine-linked cMNP was verified by detecting the peptide bond atom binding absorption bond at 3439  $\text{cm}^{-1}$  wavenumbers. This is while the cMNP's characteristic bonds were seen at their previous range (Miao et al. 2017). The folate conjugation process had passed two distinct verification FTIR analyses: The folate-putrescine-glutamine (FPG) linker and linker-cMNP conjugating steps. As shown in Fig. 4 sections C and D, the common typical characteristic band in both FPG and FLCMNP was detected at 1511.11  $\text{cm}^{-1}$ , which exhibits the presence of phenyl and pterin rings in folate structure (Mohammed 2014). However, the success in producing FPG linker was approved by detecting the folate (1511.22  $\text{cm}^{-1}$ ) (Mohammed 2014), putrescine (2847.67  $\text{cm}^{-1}$ ) (Saha et al. 2016), and glutamine (3378.44  $\text{cm}^{-1}$ ) (Miao et al. 2017). Finally, the enzyme conjugation process was proved by detecting the proteins' amino acid peptide bonds at 3000 to 3500  $\text{cm}^{-1}$  wavenumbers (Fig. 4E) (Miao et al. 2017).

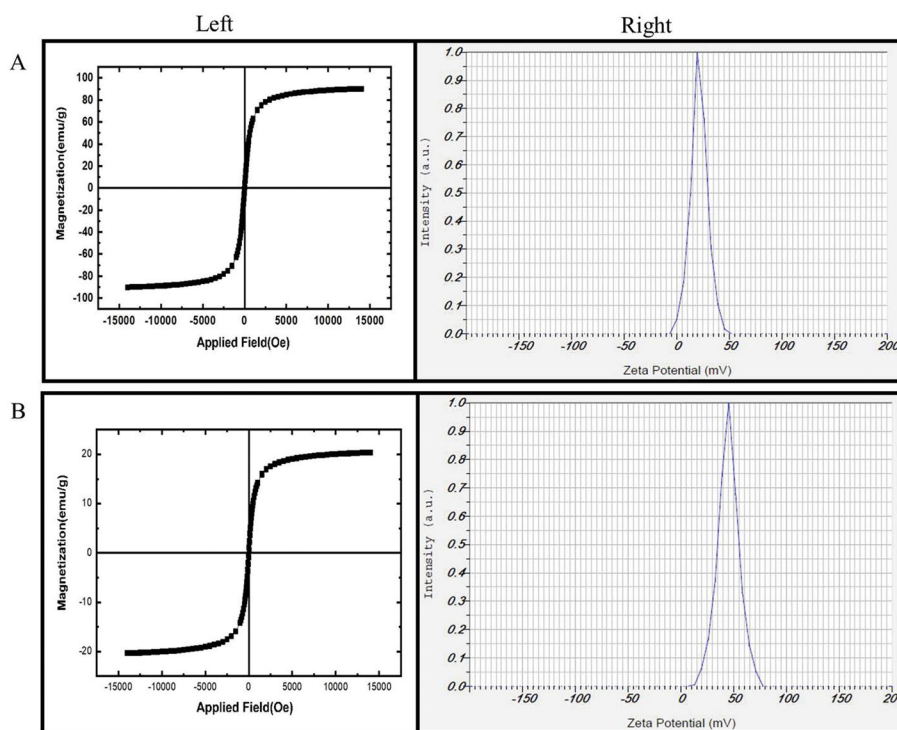


**Fig. 3** The VSM (left) and zeta potential (right) result of MNP (**A**) and hisABC (**B**); VSM vibrating sample magnetometer results, MNP magnetic nanoparticle, hisABC-NB human immune simulating anti-breast cancer-nanorobot

#### The enzyme immobilization efficiency

Also, considering the standard Bradford curve of bovine serum albumin, the ELE% was calculated at 94.76%.

#### The hisABC-NB activity

The hisABC-NB activity was compared with the un-conjugated enzymes, including both iNOS and MPO, to evaluate the impact of enzyme immobilization on their activity. As shown in Fig. 5A, the immobilized iNOS enzyme on the hisABC-NB surface exhibits more significant activity than the free enzyme. The increased activity (3.8 IU) of the conjugated iNOS compared with its un-conjugated form (2.5 IU) may indicate the enzyme condensation during the immobilization process. The constant  $K_m$  value (18  $\mu\text{M}$ ) before and after conjugating process reflects no changes in the enzyme affinity to arginine during the immobilization process (Sudo 1995). On the other hand, the decreased  $K_m$  value from 50 to 40  $\mu\text{M}$  indicates the enhanced affinity of the conjugated MPO to tyrosine (Fig. 5B). Formazan has been measured for simultaneously measuring both immobilized iNOS and MPO enzymes on the hisABC-NB surface (Fig. 5C).

The maximum hisABC-NB activity was detected at the combined concentration of tyrosine: arginine (450  $\mu\text{M}$ : 120  $\mu\text{M}$ ). Also, the hisABC-NB's functional stability was studied by plotting the nanorobot activity (Fig. 5C, D). In this regard, the half-life of hisABC-NB can be estimated at  $T_{1/2} = 5$  days, 5 h, and 39 min (Fig. 5D).

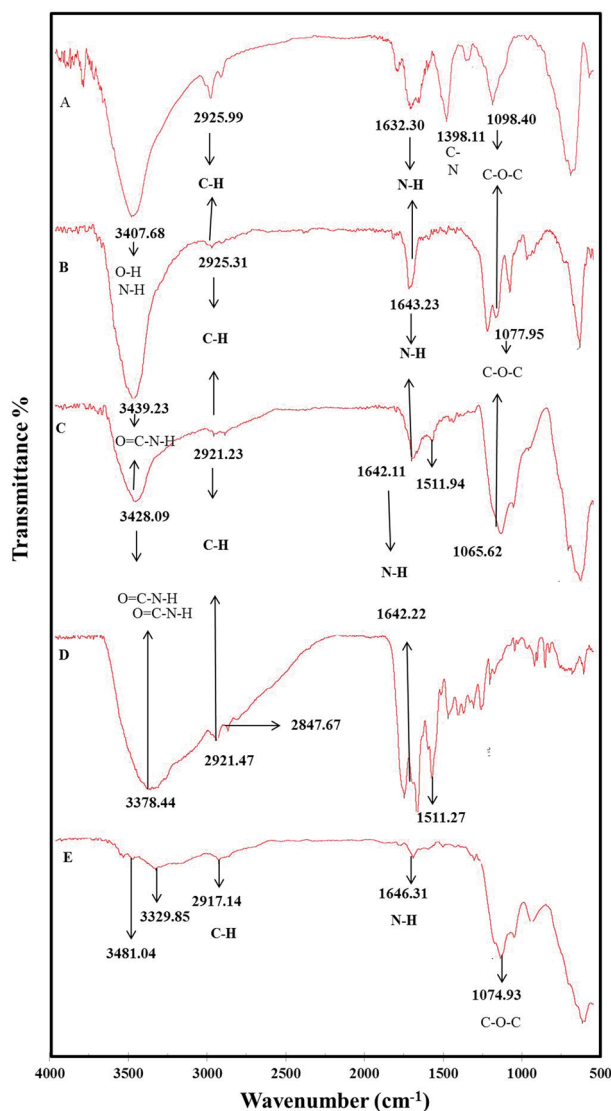


**Fig. 4** The FTIR characterization of the hisABC-NB and its sub-particles including cMNP, LcMNP, FLcMNP, and FPG; *MNP* magnetic nanoparticle, *FLcMNP* folate-linked lysine-chitosan MNP, *FPG* folate-putrescine-glutamine linker, *hisABC-NB* human immune simulating anti-breast cancer-nanorobot

**Table 1** The FTIR characteristic bands of the hisABC-NB nanomaterial

Nanomaterial	Characteristic bands	The bands' type and related atoms
cMNP	3407.68	O–H and N–H stretching vibrations
	2925.99	C–H stretching vibrations
	1632.30	N–H bending vibrations
	1098.40	C–O–C stretching vibrations
LcMNP	3439.39	N–H and O–H stretching bonds of the amino acids
FLcMNP	1511.11	Phenyl and pterin ring
FPG	2847.67	Symmetrical (ν <sub>s</sub> CH <sub>2</sub> ) stretching vibrations of the CH <sub>2</sub> groups
	1511.22	Phenyl and pterin ring
hisABC-NB	3000–3500	N–H and O–H stretching bonds of the amino acids

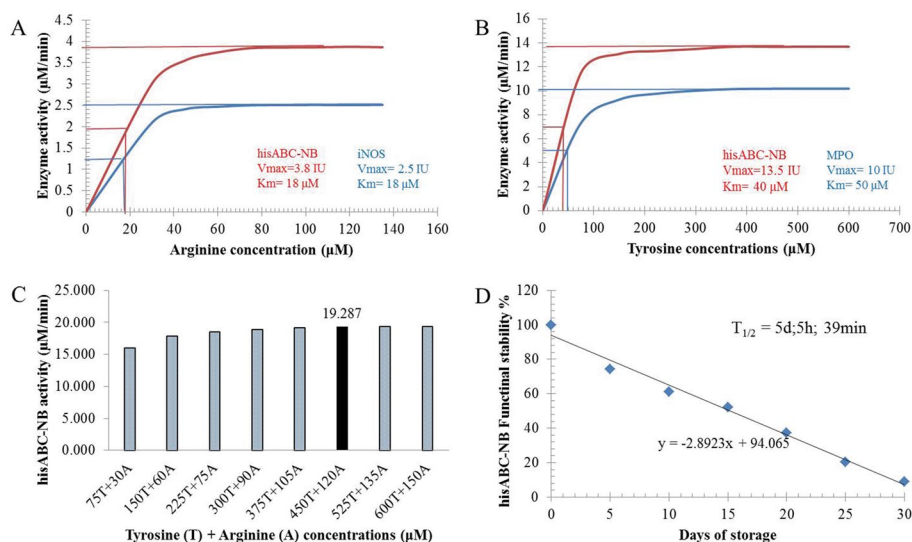


**Fig. 5** The enzyme activity and time-mediated functionality. **A** The comparative Michaelis–Menten diagram of iNOS and hisABC-NB. **B** The comparative Michaelis–Menten diagram of MPO and hisABC-NB. **C** The maximum hisABC-NB activity and its related substrate. **D** The hisABC-NB functional stability during 30 days of incubation at 4 °C; *hisABC-NB* human immune simulating anti-breast cancer-nanorobot

### The hisABC-NB selective cytotoxicity

To evaluate the hisABC-NB selective cytotoxicity, a range of hisABC-NB concentrations (0, 31.2, 62.5, 125, 250, 500, 750, and 1000 μg/ml) was added to the 2-ml cell culture dishes (6 cm) of both normal (MCF-10a) and cancerous (MCF-7) cells. The results exhibited a significant association between the increasing doses of hisABC-NB and enhanced incubation times (Fig. 6). The binding ability of hisABC-NB to the cell membrane folate receptors was verified by detecting the cellular cassette consisting of MCF-7 dead cells after 48 h of hisABC-NB treatment compared with MCF-10a cells (Fig. 6A). The survival rate of both MCF-10a and MCF-7 cells at every incubation time was greater than 65 percent at 1000 μg/ml FLcMNP concentrations (Fig. 6B). The survival rate of MCF-10a cells at every incubation time interval was greater than 50 percent at 1000 μg/ml hisABC-NB concentration. Meanwhile, low doses of hisABC-NB decreased the MCF-7 survival rate up to 50% during different incubation times (Fig. 6C). The corrected survival rate of both cell lines is presented in Fig. 6D, which distinguished only the hisABC-NB toxicity. Table 2 shows the fixed IC<sub>50</sub> concentration of hisABC-NB for 24, 48, and 72 h of incubation in normal and cancer cell lines.

### The hisABC-NB's hemolytic activity

The negligible hemolytic activity of hisABC-NB was detected during the 4 h of the blood-exposing process period (Fig. 7).

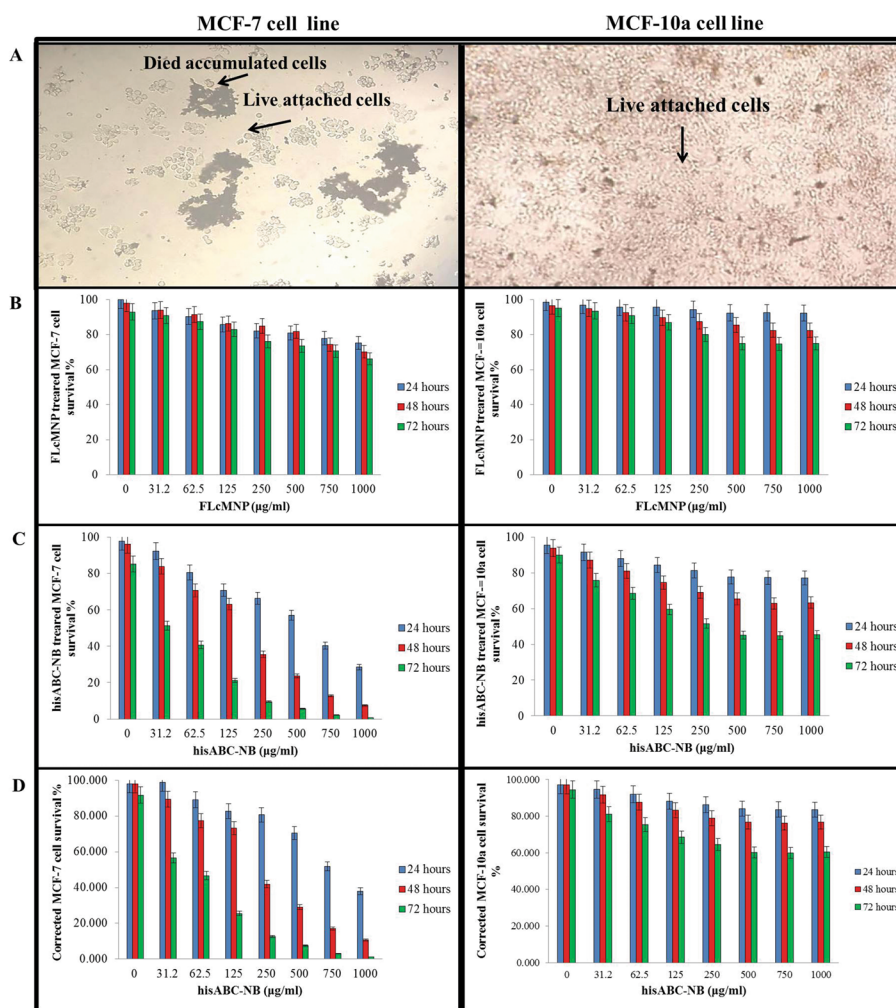


**Fig. 6** The cell survival rate and morphology of both **A** cancerous MCF-7 and **B** MCF-10a normal breast cell lines. hisABC-NB: human immune simulating anti-breast cancer-nanorobot. *FLeMNP* folate-linked lysine-chitosan MNP

**Table 2** The IC<sub>50</sub> concentration of hisABC-NB at different incubation times for MCF-7 and MCF-10a cell lines

Incubation time (hour)	IC <sub>50</sub> for MCF-7 cells (µg/ml)	IC <sub>50</sub> for MCF-10a cells (µg/ml)
24	811.09	4874.19
48	257.63	4588.81
72	87.74	1360.09

**The hisABC-NB cellular uptake results**

As shown in Fig. 8, the notable greater cellular uptake of hisABC-NB in MCF-7 cells was detected compared with normal MCF-10a cells, which can be due to the over-expressed folate receptors in the MCF-7 cell line.

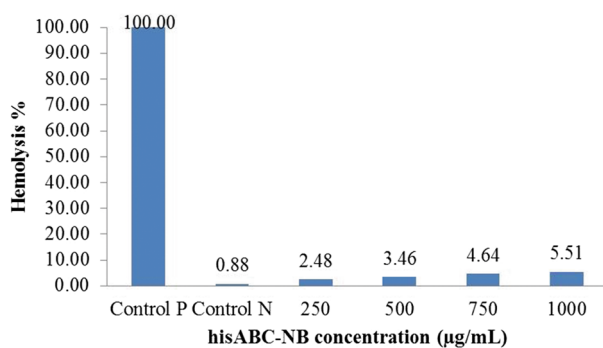


**Fig. 7** The hemolytic impact of hisABC-NB on human blood. Control P: Triton X-100, Control N normal saline, his-ABC-NB human immune simulating anti-breast cancer-nanorobot

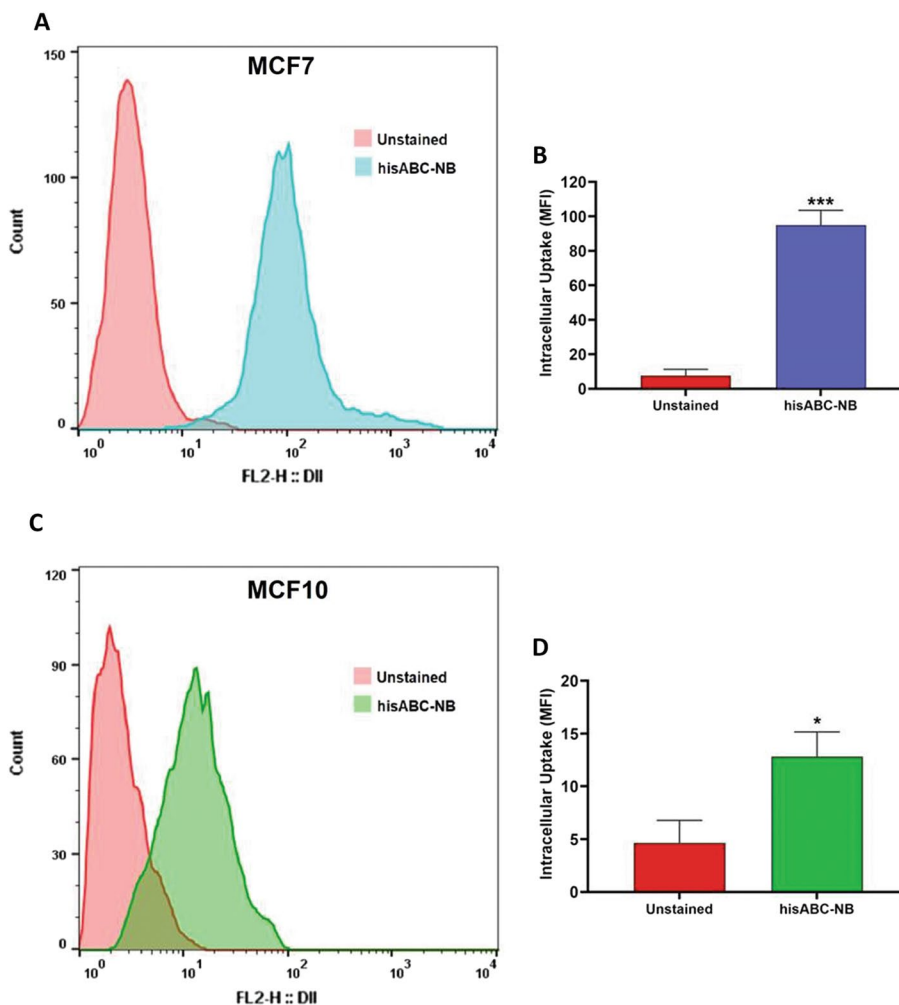


**Fig. 8** The hisABC-NB cellular uptake. Parts **A** and **B** show the hisABC-NB's cellular uptake in MCF-7 cancer cells. Parts **C** and **D** indicate the hisABC-NB's cellular uptake in normal MCF-10a cells. his-ABC-NB human immune simulating anti-breast cancer-nanorobot

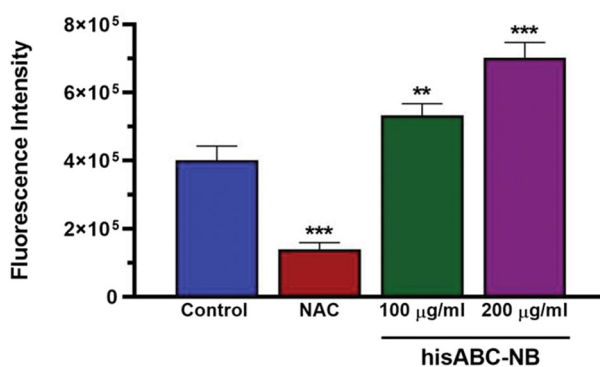


**Fig. 9** The ROS generation potential of hisABC-NB. *his-ABC-NB* human immune simulating anti-breast cancer-nanorobot

### ROS assay

The hisABC-NB significantly induces the intracellular ROS following the 100 and 200  $\mu\text{g/ml}$  treatment concentration. The results indicate the ROS-mediated cytotoxicity of hisABC-NB compared with non-treated and NAC-treated samples (Fig. 9).

### The hisABC-NB mediated cell death type

According to Fig. 10, the decreased cell survival rate following the  $\text{IC}_{50}$  dose of hisABC-NB during 24 and 48 h of incubation can be attributed to the impact of hisABC-NB on arresting the cell cycle phase at their G2/M. The increased G2/M peak exhibited the greater arrested cell population in the G2/M phase, which had not been allowed to complete the cell cycle process due to several types of ROS and RNS effectors (Park et al. 2019; Gao and Williams 2012).

In agreement with the flow cytometry results, the gene expression profile of the MCF-7 cells showed the hisABC-NB's apoptotic activity after 48 h of incubation at the related  $\text{IC}_{50}$  concentration of hisABC-NB. The BAX and P53 genes were significantly up-regulated (Fig. 11A and C). To visualize the apoptotic impact of only hisABC-NB on MCF-7 cells, the fold changes ratio was calculated by dividing it following the hisABC-NB treatment to its values after FLCMNP treatment. The comparative fold-change ratios showed a detectable up-regulation of both P53 and BAX genes after 24 and 48 h of incubation. Meanwhile, the BCL2 expression decreased after 48 h of hisABC-NB treatment (Fig. 11B and D). Moreover, the quantification results of the dead cells (Fig. 12) show the increased total population of necrotic cells in the MCF-7 cells following the FLC-MNP and hisABC-NB treatment.

### The hisABC-NB MRI-traceability

The MRI imaging revealed the hisABC-NB points in different areas of the MBC-injected models applying T2-weighted imaging. The hisABC-NB exhibited the aggregation-enhanced T2-weighted MRI contrast in their disseminated areas. In this regard, Lin et al. demonstrated that their synthesized magnetic nanoparticles increased the T2-weighted contrast of MRI imaging (Lin et al. 2009). As shown in Fig. 13, the T2-mediated MRI contrast has revealed the red and yellow points

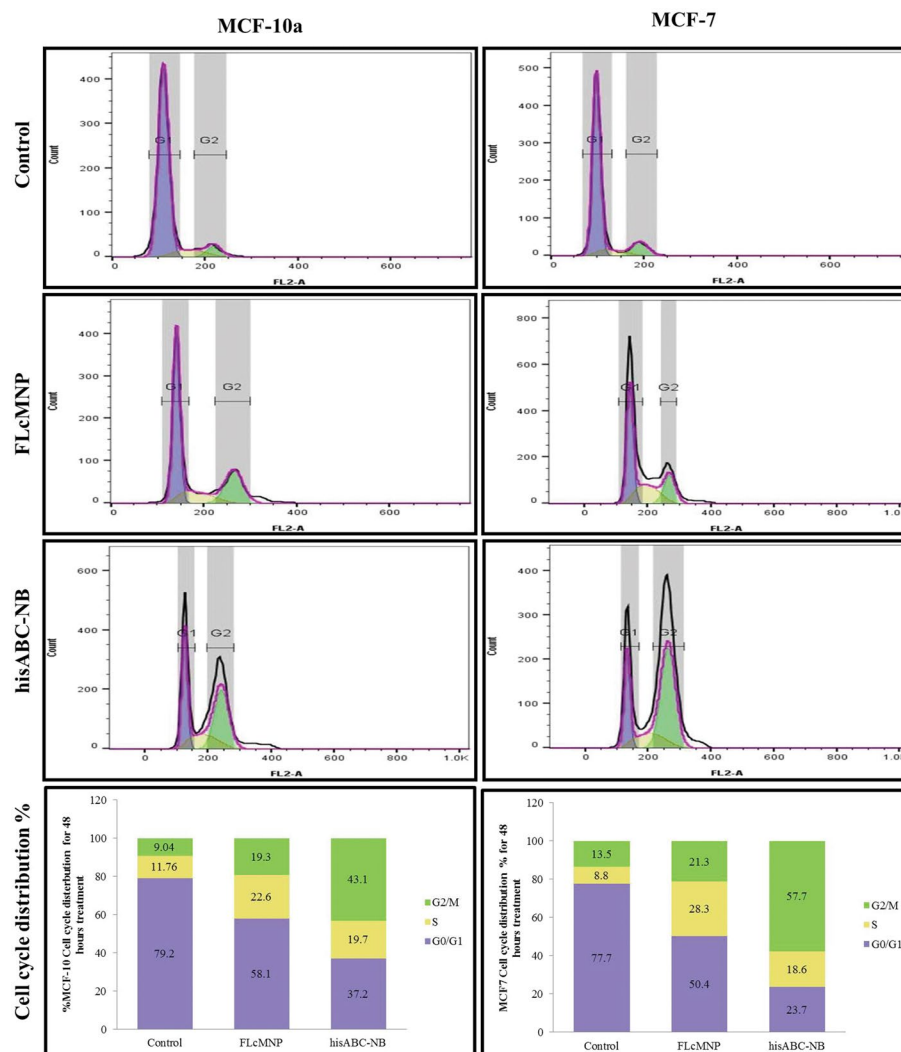


**Fig. 10** The flow cytometry result of cell cycle distribution % after treatment of both normal (MCF-10a) and cancer (MCF-7) cells with FLcMNP and hisABC-NB elements; *his-ABC-NB* human immune stimulating anti-breast cancer-nanorobot. *FLcMNP* folate-linked lysine-chitosan MNP

(Wáng and Idée 2017) in the mice's distal and proximal areas of the tumor site. The T2-weighted MRI contrast did not significantly appear in the not-injected control mice (Fig. 13A). This is while a remarkably enhanced T2-mediated MRI contrast was detectable in mice that received hisABC-NB via peritoneal (Fig. 13B) and intravenous (Fig. 13C) injections. The intravenous injection displayed the wider hisABC-NB diffusion at the tumor area compared with its central condensed less diffusion in peritoneal injection.

## Discussion

The more selective and efficient anticancer treatment strategies have opened promising horizons in increasing cancer patients' survival rates. Drug delivery systems containing the encapsulated bioactive compound have been widely applied in recent research

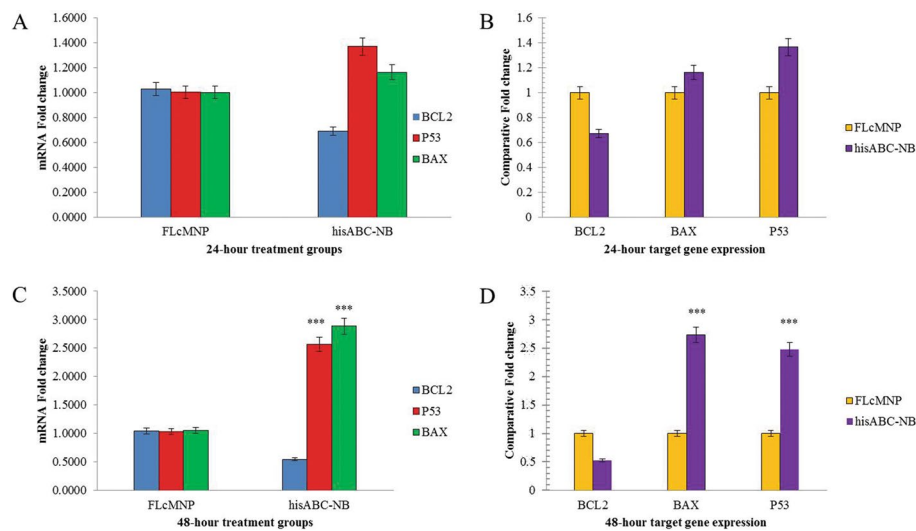


**Fig. 11** The induced gene expression profile of MCF-7 breast cancer cells mediated by hisABC-NB and FLcMNP exposure. **A** and **C** Indicate the fold change of target genes' mRNA induced by 24- and 48-h treatment of MCF-7 breast cancer cell line with hisABC-NB and FLcMNP exposure, respectively. **B** and **D** Show the comparative fold change ratio of target genes induced by 24- and 48-h treatment of both hisABC-NB and FLcMNP in MCF-7 cells. The "\*\*\*\*" shows  $p$ -value  $< 0.001$ . his-ABC-NB: human immune simulating anti-breast cancer-nanorobot; FLcMNP: folate-linked lysine-chitosan MNP

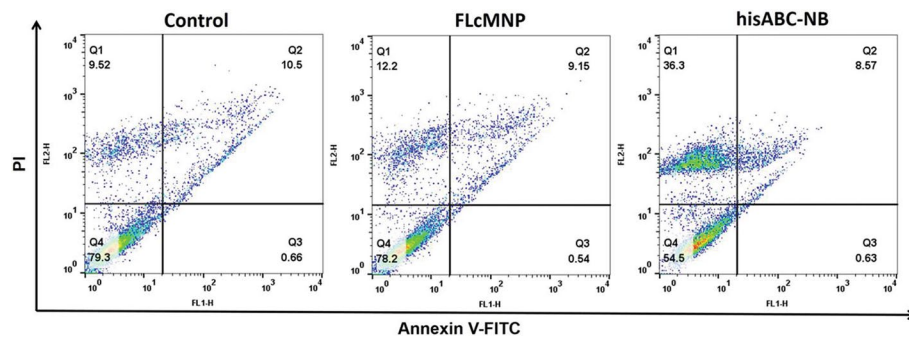


**Fig. 12** The cell death type determination following the 48-h treatment of both MCF-7 and MCF-10a cell lines with hisABC-NB. his-ABC-NB human immune simulating anti-breast cancer-nanorobot

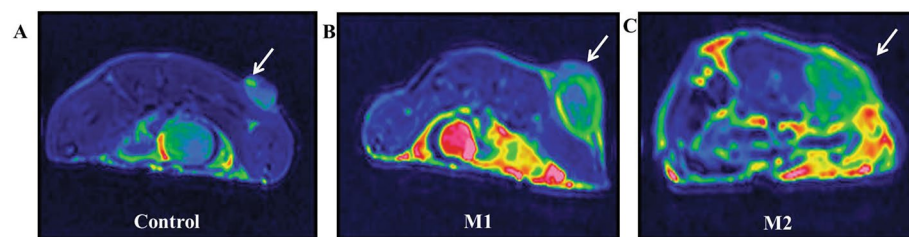


**Fig. 13** The MRI imaging of MBC models. **A** The not-injected control MBC model, which has not received hisABC-NB. **B** The MBC model received hisABC through peritoneal injection. **C** The MBC model received hisABC-NB via intravenous injection. The arrow indicates the solid tumor site; red and yellow areas reflex the improved  $T_2$ -weighted MRI contrast; MBC murine breast cancer, hisABC-NB human immune simulating anti-breast cancer-nanorobot

(Asadollahi et al. 2022; Zeinali et al. 2021; Piazzini et al. 2019; Mansoori et al. 2020). To the best of our knowledge, this is the first time producing a novel dynamic delivery system simulating the enzymatic effectors of innate immune cell response called human immune simulating anti-breast cancer-nanorobot (hisABC-NB) and analyzing its apoptotic, selectivity, cytotoxicity, and MRI-traceability.

Considering the increasing global rate of patients suffering from breast cancer (BC), early diagnosing and efficient treatment strategies have been investigated and developed to increase the BC patients' survival rate (Birnbaum et al. 2018). One of the most common mechanisms of the anticancer compounds has been assigned to their potential to produce tumor-suppressive reactive oxygen (ROS) and reactive nitrogen (RNS) species (Mitra et al. 2019). Meanwhile, the local oxidative stress at the tumor microenvironment has been reported as one of the critical tumor progressive causes. In other words, ROS plays a double-edged sword role in tumor progression and suppression process (Aboelella et al. 2021).

The tumor-caused oxidative stress (tc-OS) not only increases the anti-apoptotic and antioxidant potentials of tumor cells but also leads to tumor growth and progression to form solid tumor tissue (Gorrini et al. 2013). The tc-OS induces carcinogenesis by entrapping immune suppressor cells (Takeuchi and Nishikawa 2016). In this regard, the infiltrated cytotoxic M1 macrophages will be polarized to immune-suppressive M2 macrophages, which have lost their oxinflammation-mediated cytotoxic potential and secrete anti-inflammatory cytokines (Takeuchi and Nishikawa 2016; Zhang et al. 2013; Pan 2020). On the other hand, the excess exogenic ROS accumulation suppresses the tumor growth by activating mitochondrial-, endoplasmic reticulum-, and P53-mediated apoptotic pathways (Chakraborti et al. 2020; Huang et al. 2021). Due to the self-adaption system of tumors to ROS/RNS-mediated oxidative stress (Huang et al. 2021), the passive OS inducers only have a temporary anticancer activity upon consumption.

Herein, producing hisABC-NB made the cancer cell self-adaptive potential ineffective and induced selective apoptotic/necrotic death by continuously producing excess hypochlorous acid (HClO) and nitric oxide (NO) nearby the targeted MCF-7 cancer cells. Targeting cancer cells is mediated by binding the related ligand to their membrane receptors. In this regard, Norton et al. showed the FOLR-1 overexpression in triple-negative breast cancer patients (Norton et al. 2020). Herein, the folic acid conjugation improved the hisABC-NB selective cytotoxicity in MCF-7 cells, which can be due to their increased membrane FOLR-1 receptors (Marshalek et al. 2016; Chung et al. 1993).

Since the cells uptake folic acid in its free and conjugated forms by receptor-mediated endocytosis mechanism (Zhang et al. 2009; Zhao et al. 2014; Zhao et al. 2011), the hisABC-NB's cytotoxicity can be either caused by its non-enzymatic construction and/or enzymatic activity. The  $\text{Fe}_3\text{O}_4$  content of the non-enzymatic part of hisABC-NB can be considered the leading cause of its passive toxic impact (Sadeghi-Aliabadi et al. 2013). Meanwhile, the enzymatic part of hisABC-NB has the potential to a produce dynamic cytotoxic impact by producing ROS/RNS-mediated oxidative stress. Therefore, the cells' survival rate was evaluated for both non-enzymatic and enzymatic parts of hisABC-NB. The hisABC-NB has exhibited minor and major cytotoxic impacts on MCF-10a and MCF-7 cells, respectively. The partial decrease of MCF-10a cell survival rate can be attributed to its low FOLR-1 receptor and toxic

parts of hisABC-NB before and after the cell entrance. Therefore, the increased MCF-7 cellular death compared with MCF-10a cells verified the overexpressed FOLR-1 and the hisABC-NB selectivity. In this regard, the high cellular uptake of hisABC-NB in MCF-7 cells compared with MCF-10a type support the FOLR-1 overexpression of MCF-7 cells and receptor-mediated endocytosis mechanism of hisABC-NB, which clarifies its selective cytotoxicity (Fig. 8).

The cytotoxicity of the anticancer compounds can be related to their apoptotic activity, which induces a safe programmed death in the target cells. Among various effector genes in the cellular apoptosis pathway, the expression of the three most critical genes, including BAX, BCL-2, and P53, was analyzed following the cell treatment program at the  $IC_{50}$  concentrations of hisABC-NB and its non-enzymatic part (FLcMNP). The down-regulation of the apoptotic BAX and P53 genes (Basu and Haldar 1998) is known as the carcinogenic gene expression alteration in most cancer cells, which is required to improve the cancer cell survival and proliferation rate under stressful conditions (Pandey et al. 2016).

BAX protein is oligomerized at the outer membrane of mitochondria and mediates its permeabilization to run the powerful intrinsic cellular apoptosis pathway (Liu et al. 2016). The P53, as both extrinsic and intrinsic apoptotic effector controls, G1/S and G2/M cell cycle checkpoints, in which arrest occurs before DNA replication and mitosis, respectively. It is responsible for detecting irrecoverable genome mutations after full stress conditions such as oxidative stresses (Feroz and Sheikh 2020; Taylor and Stark 2001). On the other hand, several cancer cells have evolved to up-regulate and activate the anti-apoptotic BCL-2 gene (Suvarna et al. 2019) and down-regulate both the BAX and P53 apoptotic effectors (Basu and Haldar 1998).

Herein, the apoptosis pathways of the cancerous MCF-7 cell line were activated in both extrinsic and intrinsic routes by being exposed to the  $IC_{50}$  concentration of hisABC-NB and its non-enzymatic part (FLcMNP) for 24- and 48-h incubations. The late cellular death can be due to the cancer resistance mechanisms of cell survival and cancer oxidative buffering ability, which was defeated after a 48-h continuous oxidants' flow produced by immobilized iNOS and MPO enzymes.

The significant overexpression of both BAX and P53 genes reflex the cell resistance defeat and induction of P53-mediated apoptotic death by arresting them in the G2/M phase. The cell cycle distribution data indicated the P53-mediated apoptosis in MCF-7 cells by increasing the G2 arrested cell population after 48-h incubation following the FLcMNP and hisABC-NB treatment. On the other hand, p53 can also cause necrotic cell death following ROS-mediated DNA damage by conducting the activation of lysosomal cysteine protease cathepsin Q (Ying and Padanilam 2016). In this regard, as shown in Fig. 12 the notable increase in the Q1 section of the Annexin V-FITC/PI diagram following the hisABC-NB treatment compared with FLcMNP and control measurements, not only verified the folate receptor-mediated endocytosis mechanism of hisABC-NB cytotoxicity, but also clarified the necrotic potential of the hisABC-NB activity.

Also, the ROS- and nitric oxide-mediated oxidative stresses are critical in mediating the cell cycle arrest at the G2/M phase (Park et al. 2019; Gao and Williams 2012).

## Conclusion

Investigating a combined complex compound consisting of both inflammatory and oxidative stress inducers makes an efficient oxinflammation-mediated cytotoxic impact on cancer cells. In the current study, synthesizing a cancer cell-selective dynamic ROS/RNS nano-generator robot (hisABC-NB) has provided an efficient immune response alternate for cancer therapy strategies. The magnetism property of hisABC-NB makes it traceable by detecting the intensified T2-weighted MRI contrast and magnet-navigable during the treatment process. Moreover, the magnet-mediated easy safe manual clearance of hisABC-NB enhances its potential to be used as the first modern anticancer tool. However, further in vitro and in vivo experimental studies must be conducted to verify its selective cytotoxicity and its possible crosstalk interactions with the immune response net.

## Methods

### Materials

Iron (II) chloride tetrahydrate ( $\text{FeCl}_2 \cdot 4\text{H}_2\text{O}$ ), Iron (III), chloride hexahydrate ( $\text{FeCl}_3 \cdot 6\text{H}_2\text{O}$ ), acetic acid ( $\text{CH}_3\text{COOH}$ ), and ammonium hydroxide ( $\text{NH}_4\text{OH}$ , 37%), were obtained from Merck, Germany. Ketamine (10%) and xylazine (2%) were prepared from Medistar and Riemser pharma companies (Germany), respectively. N-acetyl cysteine (NAC) (Cayman, USA), fluorescein-5-isothiocyanate (FITC) (Sigma-Aldrich), chitosan (LMW, 85% deacetylated), lysine, putrescine, tyrosine, arginine, folic acid, NADPH, MTT, transglutaminase (TGase, from guinea pig liver, code: T5398), nitric oxide synthase (iNOS, inducible from mouse, code: n2783), myeloperoxidase (MPO from human leukocytes, code: m6908), 1-Ethyl-3-(3-dimethylaminopropyl) carbodiimide (EDC), nicotinamide adenine dinucleotide phosphate (NADPH) were purchased from Sigma-Aldrich Company at Chemie GmbH Eschenstrasse 5D-82024 Taufkirchen.

### The magnetic nanoparticle (MNP) synthesis

The MNPs were synthesized by applying the simple high-performance base-mediated precipitation methodology, which is followed as follows:



Briefly, the 450-ml solutions of ferrous chloride and ferric chloride were prepared with distilled water and mixed in 1:2 molar proportions. The 900-ml mixed solution was heated up to 66 °C for 10 min under stirring conditions. Then, the  $\text{Fe}_3\text{O}_4$  nanoparticles were gradually precipitated by dropwise insertion of 100 ml  $\text{NH}_4\text{OH}$  solution (32%) under the same thermal and stirring conditions. Finally, the black-colored precipitate was collected by a strong 1.5-T neodymium magnet and washed several times for removing the non-reacted participants during the reaction process. The pure  $\text{Fe}_3\text{O}_4$  magnetic nanoparticles were stored in deionized water at 4 °C (Kulkarni et al. 2012).

### The MNP functionalization

#### Chitosan coating

A high-performance ultrasonication method was applied to prepare the most reactive surface for MNP nanoparticles. The MNPs were added into the 450 ml acetic acid solution (2%V/V) containing the solved low molecular chitosan (1%W/V) under 350 W

power probe sonication for 30 min (8 s on:2 s off). The final thermal condition was regulated to less than 72 °C. Then, a shaker incubator was utilized for continued shaking of the homogenized solution at 50 °C for 18 h. The chitosan-coated nanoparticles (cMNPs) were magnetically extracted and rinsed with deionized water.

#### ***Folate conjugating and enzyme immobilization***

The product synthesizing program was designed in three main steps: The pre-modification, pre-functionalization, and final-functionalization phases. In the pre-modification step, the cMNP surface was decorated with lysine by applying the EDC-mediated isopeptide bond formation between the chitosan amine groups and the lysine's carboxylic terminal. Briefly, the 20 ml of lysine solution (1 M), 20 ml deionized water, 5 ml of cMNP suspension (10 mg/ml), and 5 ml ethyl-3-[3-(dimethylamino)propyl]-carbodiimide (EDC) solution (0.1 M) were added to the last solution. A 2% acetic acid solution was used to adjust the reaction pH to 6 to increase the EDC activity. Then, the suspension was incubated at 30 °C in a shaker incubator for 12 h. Next, the lysine-decorated cMNP (LcMNP) was magnetically collected and rinsed with deionized water. The LcMNP concentration was calculated in 1 ml of deionized water and stored at 4 °C.

In the pre-functionalization phase, the folate molecule was linked to putrescine and lysine to be competent for being detected as the folate receptor ligand. In this regard, folate (10 µg/ml), putrescine (2 mg/ml), and lysine (1 mg) were mixed at a proportion of 100:1:1 (ml) to avoid non-desired linkages. Then, the mixture pH was adjusted to 6 with acetic acid. Finally, the EDC solution (0.1 M) was dropwise added to the solution and incubated at 30 °C in a shaker incubator for 12 h. The folate-conjugated linker was extracted by 12,000 RPM centrifuging and purified by three times rising by deionized water.

The enzyme/folate-decorated LcMNP, called human immune cell simulated anti-breast cancer-nanorobot (hisABC-NB), was produced in the final-functionalization phase. In this regard, the folate linkers (2 mg/ml), LcMNP (4 mg/ml), and enzymes master mix (iNOS + MPO) (4 mg/ml) were added together. The enzyme master mix was prepared by mixing 2 mg of both iNOS and MPO enzymes in a 50 ml phosphate buffer solution (PBS, pH 7). The third step was finalized by adding 2 mg transglutaminase (TGase) to link both folate linkers and enzymes pack to LcMNP. The conjugation process was conducted by 20 min of incubation at room temperature under continuous stirring. Finally, the synthesized hisABC-NB was magnetically collected and rinsed with PBS (Fig. 1).

#### **The conjugation efficiency measurement**

##### ***The enzymes immobilization efficiency (%EIE)***

To evaluate the %EIE, both iNOS and MPO were incubated in the presence of FLcMNP and TGase, as described in “[The hisABC-NB activity](#)” section. The %EIE was determined by estimating the protein concentration before and after incubation. The protein concentration was measured by preparing the bovine serum albumin (BSA) standard concentration curve by applying the Bradford assay analysis. The sample protein concentration was estimated before and after the conjugating incubation process considering

the plotted BSA protein standard curve. Finally, the % EIE was calculated as the following equation (Eq. 1):

$$\%EIE = \frac{[SPC]b - [SPC]a}{[SPC]b} \times 100, \quad (1)$$

where the [SPC]a and [SPC]b indicate the sample protein concentration after and before the incubation process.

### Characterization of MNP and its functionalized forms

The MNPs' crystal property was conducted by X-ray diffraction (XRD) analysis utilizing X-ray diffractometer (Philips PW 1730/10). The diffractogram was plotted by applying Cu-K $\alpha$  radiation ( $\lambda$ 1.5406 Å) in the range  $10^\circ < 2\theta < 80^\circ$  with steps of 0.05 at room temperature (Silva et al. 2013). The MNPs' magnetic properties were analyzed by vibrating sample magnetometer (VSM) systems equipped with a superconducting quantum interference device (SQUID) sensor. The measurements were taken at 25 °C in magnetic fields ranging from  $-15$  to  $+15$  kOe. Fourier transform infrared spectroscopy (FTIR) was utilized to detect the chitosan, lysine, and folate functional groups, which approve the FLcMNP formation. Moreover, the individual structural properties of the immobilized enzymes were identified by FTIR analysis. The spectra were plotted over the range of  $(400-4000)$   $\text{cm}^{-1}$  wave numbers by an FTIR spectrophotometer. To determine the size of hisABS-NBs, they were prepared for being studied by field emission scanning electron microscope. For FESEM imaging, the MNP and hisABC-NB samples were dried on gold-coated silicon and fixed with sticky carbon tape. The images were recorded at 5 kV voltages applying a (Carl Zeiss ultra 55 Field-Emission Scanning Electron Microscope). Also, TEM images of the hisABC-NB specimens were obtained using a 200 kV transmission electron microscope (JEM-ARM200F) equipped with aberration correctors. Moreover, the hisABC-NB size was measured by the dynamic light scattering method (DLS) to approve the FESEM results. Finally, the hisABC-NB structural stability was analyzed by measuring their surface electric charge called zeta potential.

### The hisABC-NB enzyme activity

#### *The hisABC-NB enzymatic kinetics*

The iNOS enzyme produces nitric oxide by catalysis of arginine in the presence of NADPH co-enzyme. On the other hand, the MPO enzyme produces radical tyrosine by the catalysis of tyrosine (Heinecke et al. 1993). It is well-known that nitric oxide and radical tyrosine have the potential to be used as reductive agents (Bartberger et al. 2002). To measure the enzymes' production, a chlorogenic agent like the yellowish 3-(4,5-dimethylthiazol-2-yl)-2,5-diphenyl tetrazolium bromide (MTT) compound, which in its reduced form changes its color to insoluble violet formazan. Therefore, measuring the UV-visible absorbance of the formazan production at 570 nm indicates the iNOS and MPO individual productions (Liu et al. 2009). Briefly, different concentrations of arginine (30, 45, 60, 75, 90, 105, 120, and 135  $\mu\text{g/ml}$ ) and tyrosine (75, 150, 225, 300, 375, 450, 525, and 600  $\mu\text{g/ml}$ ) were prepared for measuring the iNOS and MPO activity, respectively. Due to the NADPH reductive potential, the NADPH was used at a constant final concentration of 100  $\mu\text{M}$ . The enzyme assay cuvette contains PBS, hisABS-NB,

substrates, and MTT dye (0.5 mg/ml). The final volume of the reaction phase was set at 500  $\mu$ l. The blank cuvette had no hisABC-NB calibrated for the reaction participants. To evaluate the enzyme activity of iNOS, MPO, and iNOS/MPO separately, the reaction substrates were individually utilized depending on the desired enzyme. The enzyme standard curves were plotted by estimating the productions' concentration during 1-min enzyme activity to plot the Michaelis–Menten diagram of the selected enzymes.

#### **The hisABC-NB functional stability**

The enzyme activity of the hisABC-NB was measured every 5 days for 30 days.

#### **Cell culture**

Both breast cancer (MCF-7) and normal (MCF-10a) cells were purchased (Pasture Institute, Tehran, Iran) and seeded at  $7 \times 10^4$  cells/cm<sup>2</sup> density in T-25 cell culture flasks and cultured at 95% humidity, 5% CO<sub>2</sub>, and 37 °C conditions. The MCF-7 cells were cultured in a DMEM cell culture medium (Gibco), which was supplemented by FBS (10%), streptomycin (100 mg/ml), and penicillin (100 U/ml). The MCF-10a cells were cultured in DMEM/Ham's F-12 (GIBCO-Invitrogen, Carlsbad, CA) supplemented with 20 ng/ml epidermal growth factor (EGF), 100 ng/ml cholera toxin, 500 ng/ml hydrocortisone, 0.01 mg/ml insulin, and 5% Chelex-treated horse serum, which was all purchased from Sigma (St. Louis, MO, USA).

#### **The hisABC-NB's cytotoxicity assay**

Considering the potentially reductive activity of the hisABC-NB, the common MTT assay could not evaluate its cytotoxicity on breast cancer and normal cell lines. Therefore, the dye exclusion test was used to study the hisABC-NB cytotoxicity by determining the present viable cells' count in a cell suspension. The viable cells were detected with their clear cytoplasm, and non-viable cells were observed with blue cytoplasm.

In this regard, the cultured MCF-7 and MCF-10a cells were treated with different concentrations of hisABC-NB (250, 500, 750, and 1000  $\mu$ g/mL) and incubated for 24, 48, and 72 h. The cell media was refreshed after 20-min incubation to allow hisABC-NB attachment to cells' folate receptors and remove not-attached nanorobots just before the incubation. To distinguish the possible toxicity of the hisABC-NB's structural skeleton (FLcMNP), it was exposed to both cell lines and the hisABC-NB treatment program.

To measure the cell survival rate, the extracted cells were re-suspended with 1 ml PBS and mixed with 1 ml filtered 0.4% trypan blue. The mixture was incubated for 3 min at room temperature. The cells were immediately counted for 3 min. The unstained (viable) and stained (non-viable) cells were counted separately to obtain the total count of viable cells in 1 ml of aliquot sample. The survival percentage was calculated as the following equation (Eq. 2) (Strober 2015):

$$\% \text{Survival} = \frac{[\text{Total live cells counted per 1 ml of aliquot}]}{[\text{Total cells counted per 1 ml of aliquot}]} \times 100. \quad (2)$$

Considering the possible cytotoxicity of the free-enzyme hisABC-NB scaffold (control), the corrected survival percentage was calculated as the following equation (Eq. 3):

$$\% \text{Corrected survival} = \left( 1 - \frac{[\text{SPc}\% - \text{SPt}\%]}{[\text{SPc}\%]} \right) \times 100. \quad (3)$$

### ROS assay

To examine the intracellular levels of ROS produced by hisABC-NB in MCF-7 cancer cells, the DCFDA/H2DCFDA-cellular ROS detection kit (Abcam, United Kingdom) was utilized (Memari et al. 2022). Briefly, the 24-h cultured MCF-7 cells ( $3 \times 10^3$ ) were washed using 1X PBS buffer and incubated with H2DCFDA solution (25  $\mu\text{M}$ ) for 45 min in dark conditions. Then, the cells were exposed to hisABC-NB (100 and 200  $\mu\text{g}/\text{ml}$  concentrations) and N-acetyl cysteine (NAC) (Cayman, USA) for 48 h. The intracellular levels of ROS were estimated by recording the fluorescence excitation and emission at 485 and 535 nm wavelengths, respectively (Victor X5 Multipliable Plate Reader (PerkinElmer, USA)).

### Intracellular reactive oxygen species (ROS) assay

In this method,  $25 \times 10^3$  SH-SY5Y cells were seeded in 6-well plates and incubated for 5 h. The cells were then treated with non-toxic concentrations of Urolithin B, which had a protective effect (0.6, 2.5, and 5  $\mu\text{M}$ ), and after 24 h, the cells were washed and incubated for 1 h with H2DCFDA solution (25  $\mu\text{M}$ ) in the dark place. After rewashing, the cells were treated with QA at a concentration of 6 mM along with the mentioned concentrations of Urolithin B for 4 h. The untreated cells were used as a negative control, and N-acetyl cysteine (NAC) (10 mM) was also used as a positive control to reduce ROS production. Finally, the fluorescence was measured (Excitation/Emission: 485/535 nm) by the fluorescence plate reader FACScan (Becton Dickinson, San Jose, USA). All the samples were tested in triplicate.

### Flow cytometry assay

The MCF-7 cells were incubated at their related  $\text{IC}_{50}$  concentration of hisABC-NB for 24 and 48 h. Then,  $1 \times 10^6$  cells were counted and re-suspended in 70% cold ethanol. The cells were fixed for 30 min at 4  $^{\circ}\text{C}$ , washed two times to remove ethanol, and treated with ribonuclease. Finally, propidium iodide (PI) (50  $\mu\text{g}/\text{ml}$ ) was added to the cell's pellets in dark conditions. The cell suspensions were incubated at room temperature for 30 min in dark conditions. The cells' frequency in different cell cycle phases was studied by utilizing a FACScan laser flow cytometer.

The apoptotic cell quantification was conducted by FITC Annexin V Apoptosis Detection Kit to determine the cell death type with PI (BioLegend, CA, USA). Briefly, MCF-7 cells were seeded in 6-well plates and cultured for 24 h at 37  $^{\circ}\text{C}$ . Then, the cells were exposed to 200  $\mu\text{g}/\text{mL}$  of both FLcMNP and hisABC-NB suspensions for 48 h. The cells were harvested and re-suspended in 100  $\mu\text{l}$  Annexin-V binding buffer. In continuation, the FITC Annexin V (5  $\mu\text{l}$ ) and PI solutions (10  $\mu\text{L}$ ) were added to the cells and incubated for 15 min at 25  $^{\circ}\text{C}$  in dark conditions. Finally, Annexin-V binding buffer (400  $\mu\text{l}$ ) was added to the samples to be analyzed by flow cytometry technique.

### Gene expression profile

The MCF-7 breast cancer cell line was exposed to the IC<sub>50</sub> concentration of hisABC-NB for 24 and 48 h incubation compared with fLcMNP as the control group. Then, the treated cells were rinsed, harvested, and lysed to extract their total RNA by applying an RNA extraction kit (Qiagen, Hilden, Germany). Next, the cDNA libraries of the sample groups were synthesized utilizing the cells' total RNA and the high-quality Quantitect Reverse Transcription kit (Qiagen, Hilden, Germany). The primers of target genes (BAX, BCL2, and P53) were designed by Allele-ID6 software to detect their expression status (Table 3). A Bio-Rad CFX96 system was utilized for the amplification of target cDNAs. An SYBR green-supplemented PCR master mix (Qiagen, Hilden, Germany) was used for conducting the real-time PCR process. The GAPDH expression as the internal gene expression control was measured to normalize the gene expression analysis by plotting the comparative threshold cycle (CT) curve. Moreover, the PCR efficiency was estimated by measuring the expression of serial dilutions of target cDNAs (Table 3).

### Hemolytic activity measurements

The hisABC-NB hemolytic activity was analyzed considering Vuddanda et al. protocol (Vuddanda et al. 2014; Huang et al. 2016). The Human red blood cells (RBCs) were separated by centrifuging at 2000 rpm for 5 min and rinsed with normal saline (0.9% NaCl) three times. The RBCs were re-dispersed in 750 µL normal saline solution. Then, a range of hisABC-NB concentrations (250, 500, 750, and 1000 µg/mL) was provided with normal saline solution separately. To evaluate the hemolytic activity of hisABC-NB, 250 µL of each concentration was added to the RBC solutions and gently shaken every 20 min for 4 h at room temperature. The 100% lysis positive control and 0% lysis negative control was prepared by inserting Triton X-100 (2% aqueous solution) and normal saline into the RBCs samples, respectively. Finally, the supernatants of centrifuged RBC were separated and incubated for 30 min at room temperature to complete the hemoglobin oxidation process. The absorbance of oxyhemoglobin was recorded at 540 nm. The RBC hemolysis rate was calculated as the following equation:

$$\text{Hemolysis\%} = \frac{(\text{OD})_s - (\text{OD})_{nc}}{(\text{OD})_{pc} - (\text{OD})_{nc}} \times 100.$$

The (OD)<sub>s</sub>, (OD)<sub>pc</sub>, and (OD)<sub>nc</sub> parameters are the absorbance of the sample, positive control, and negative control experiments (N = 3).

**Table 3** The sequence of desired primer sets

	Forward primer sequence	Reverse primer sequence
GAPDH	5' CCATCACCATCTTCC 3'	5' AATTCGTTGTCATACC 3'
BCL2	5' TAACGGAGGCTGGGATGC 3'	5' AGGTTCTGCGGACTTCGG 3'
BAX	5' GGAGCGGCGGTGATGG 3'	5' CCTGGATGAAACCTGAAGC 3'
P53	5' CCAGAATGCCAGAGG 3'	5' CAGTCAGAGCCAACC 3'

### The hisABC-NB's cellular uptake

The efficiency of hisABC-NB's cellular uptake was performed by applying flow cytometry analysis (Ge et al. 2009). To this purpose, the FLcMNP nanoparticles were modified by conjugating with FITC. In this regard, 10 mg of FITC was mixed with 10 ml of methanol. Then, the FITC solution was added to 10 ml of FLc-MNP suspension (2 mg/mL) in an acidic condition (pH 5) and incubated for 3 h under continuous stirring conditions at room temperature. Finally, the FITC-labeled FLcMNP (FFLcMNP) was separated by a strong magnet and rinsed three times to remove non-linked FITC. In the second step, both the MCF-10a and MCF-7 cells were seeded in two 6-well plates at a density of  $1.5 \times 10^6$  cells per well and cultured as described in "Cell culture" section for 24 h. The culture mediums were refreshed with fresh medium containing FFLcMNP (1 mg) and then incubated for 2 h at 37 °C. The cells were rinsed with cold PBS solution, harvested, centrifuged, and re-suspended in 250  $\mu$ l staining buffer (2% FBS + PBS). Finally, the samples were provided for flow cytometry analysis (BD FACS Calibur™, San Jose, USA). FlowJo software (v10, FlowJo, Ashland, USA) was applied to analyze data.

### Preparation of murine breast cancer model (MBC) and treatment program

To prepare a murine breast cancer model, 3 Balb/c mice (aged 5 to 7 weeks) were purchased from the Pasteur Institute of Iran. The mice were raised under sterile and standard conditions. The standard conditions are 60% relative humidity, 25 °C temperature, and 12 h light/12 h dark cycle program. One million murine 4T1 breast cancer cells were suspended by PBS solution. The cell suspension was injected into the mice's thigh muscles. After two weeks, a solid tumor appeared. The treatment program was run by adding 1 ml hisABC-NB (1 mg/ml) into 9 ml PBS (pH 7.4) and incubating for 10 min at 37 °C. Then, 50  $\mu$ l of hisABC-NB was injected into different sites of MBC. In this regard, the MBC was divided into 3 classes: The control, M1 and M2. The control was not injected. Meanwhile, the M1 and M2 classes received the peritoneal and intravenous injections, respectively. Finally, the injected mice were anesthetized after 30 min just before preparing for MRI imaging.

### MRI imaging

Magnetic resonance imaging (MRI) was carried out through a 3.0 Tesla unit GE discovery 750<sup>Gem</sup> MRI scanner with 16 element phased-array flex coil. To study the in vivo MRI, the prepared MBCs were anesthetized during the scanning period by intraperitoneal injection of the anesthetizing compound, which was prepared by combining ketamine 10% (100 mg/ml) and xylazine 2% (20 mg/ml) at 2:1 proportion. 30  $\mu$ l of the anesthetic compound was injected into the right lower quadrant of the abdomen. The mice received 0.2 mg xylazine and 2 mg ketamine regardless of weight. The treated mice were anesthetized just before MRI scanning. Then, the injected hisABC-NB at the mice's tumor region was concentrated at the tumor sites by exposing them for 10 min near a strong 1.5-T magnet. The MRI protocol included T2-weighted axial applying the FRFSE-XL method. The parameters of MRI scanning were adjusted as follows:

Slice thickness: 1.5 mm / gap: 0.10 mm, auto-repeat time (TR): 3000 – 6000 ms, echo time (TE) = 85 ms, field of view (FOV): 8 × 8, matrix: 224 × 224, bandwidth (BW) = 20.8 Hz, echo train length (ETL) = 12).

### Statistical analysis

The statistical analysis was conducted using SPSS 21 statistical package (SPSS, Chicago, IL). The one-way ANOVA test defined the  $P < 0.001$  as the statistically significant level.

### Acknowledgements

The authors appreciate the support provided by the Research and Technology Council of the Ferdowsi University of Mashhad, Iran (Grant number: 3/50636, 1398/06/26).

### Author contributions

SMRS and AA designed, conducted, analyzed, interpreted, and drafted the current study. MD critically revised and finally approved the manuscript to be published. All authors read and approved the final manuscript.

### Funding

The article publication price will be paid by own authors.

### Availability of data and materials

The datasets used and/or analyzed during the current study are available from the corresponding author upon reasonable request.

### Declarations

#### Ethics approval and consent to participate

The Research Ethics Committee of the Ferdowsi University of Mashhad approved the study by issuing an ethics code: IR.UM.REC.1401.059.

#### Consent for publication

Not applicable.

#### Competing interests

The authors declare that they have no competing interests.

Received: 1 August 2022 Accepted: 1 December 2022

Published online: 13 December 2022

### References

- Aboeella NS et al (2021) Oxidative stress in the tumor microenvironment and its relevance to cancer immunotherapy. *Cancers* 13(5):986
- Ali M et al (2022) Myeloperoxidase exerts anti-tumor activity in glioma after radiotherapy. *Neoplasia* 26:100779–100779
- Alibolandi M et al (2016) Dextran-poly lactide-co-glycolide polymersomes decorated with folate-antennae for targeted delivery of docetaxel to breast adenocarcinoma in vitro and in vivo. *J Control Release* 241:45–56
- Arfin S et al (2021) Oxidative stress in cancer cell metabolism. *Antioxidants* 10(5):642
- Asadollahi L et al (2022) Co-Delivery of erlotinib and resveratrol via nanostructured lipid Carriers: a synergistically promising approach for cell proliferation prevention and ROS-Mediated apoptosis activation. *Int J Pharm* 624:122027
- Bartberger MD et al (2002) The reduction potential of nitric oxide (NO) and its importance to NO biochemistry. *Proc Natl Acad Sci* 99(17):10958–10963
- Basu A, Haldar S (1998) The relationship between Bcl2, Bax and p53: consequences for cell cycle progression and cell death. *Mol Hum Reprod* 4(12):1099–1109
- Birnbaum JK et al (2018) Early detection and treatment strategies for breast cancer in low-income and upper middle-income countries: a modelling study. *Lancet Glob Health* 6(8):e885–e893
- Chakraborti S, Ray BK, Roychoudhury S (2020) Handbook of oxidative stress in cancer: mechanistic aspects. Springer, Cham
- Cheung A et al (2016) Targeting folate receptor alpha for cancer treatment. *Oncotarget* 7(32):52553–52574
- Chung KN et al (1993) Stable transfectants of human MCF-7 breast cancer cells with increased levels of the human folate receptor exhibit an increased sensitivity to antifolates. *J Clin Invest* 91(4):1289–1294
- Feroz W, Sheikh AMA (2020) Exploring the multiple roles of guardian of the genome: P53. *Egypt J Med Hum Genet* 21(1):49
- Gao L, Williams JL (2012) Nitric oxide-donating aspirin induces G2/M phase cell cycle arrest in human cancer cells by regulating phase transition proteins. *Int J Oncol* 41(1):325–330
- Ge Y et al (2009) Fluorescence modified chitosan-coated magnetic nanoparticles for high-efficient cellular imaging. *Nanoscale Res Lett* 4(4):287–295

- Gorrini C, Harris IS, Mak TW (2013) Modulation of oxidative stress as an anticancer strategy. *Nat Rev Drug Discovery* 12(12):931–947
- Gupta A, Shridhar K, Dhillion P (2015) A review of breast cancer awareness among women in India: cancer literate or awareness deficit? *Eur J Cancer* 51(14):2058–2066
- Heinecke JW et al (1993) Tyrosyl radical generated by myeloperoxidase catalyzes the oxidative cross-linking of proteins. *J Clin Invest* 91(6):2866–2872
- Huang H et al (2016) An evaluation of blood compatibility of silver nanoparticles. *Sci Rep* 6(1):1–15
- Huang R et al (2021) Dual role of reactive oxygen species and their application in cancer therapy. *J Cancer* 12(18):5543
- Jahan S, Karim ME, Chowdhury EH (2021) Nanoparticles targeting receptors on breast cancer for efficient delivery of chemotherapeutics. *Biomedicine* 9(2):114
- Kee HJ, Cheong J-H (2014) Tumor bioenergetics: an emerging avenue for cancer metabolism targeted therapy. *BMB Rep* 47(3):158
- Kim B et al (2020) Engineering peptide-targeted liposomal nanoparticles optimized for improved selectivity for HER2-positive breast cancer cells to achieve enhanced in vivo efficacy. *J Control Release* 322:530–541
- Lin J-J et al (2009) Folic acid–Pluronic F127 magnetic nanoparticle clusters for combined targeting, diagnosis, and therapy applications. *Biomaterials* 30(28):5114–5124
- Liu R-H et al (2009) General spectroscopic protocol to obtain the concentration of the superoxide anion radical. *Ind Eng Chem Res* 48(20):9331–9334
- Liu Z et al (2016) Direct activation of bax protein for cancer therapy. *Med Res Rev* 36(2):313–341
- Mansoori B et al (2020) Hyaluronic acid-decorated liposomal nanoparticles for targeted delivery of 5-fluorouracil into HT-29 colorectal cancer cells. *J Cell Physiol* 235(10):6817–6830
- Marshalek JP et al (2016) Intracellular delivery and ultrasonic activation of folate receptor-targeted phase-change contrast agents in breast cancer cells in vitro. *J Control Release* 243:69–77
- Memari F et al (2022) Tumor-inhibitory effects of zerumbone against HT-29 human colorectal cancer cells. *Int J Toxicol*. <https://doi.org/10.1177/10915818221104417>
- Miao Y et al (2017) Poly (L-lysine) modified zein nanofibrous membranes as efficient scaffold for adhesion, proliferation, and differentiation of neural stem cells. *RSC Adv* 7(29):17711–17719
- Milane L, Duan Z-F, Amiji M (2011) Pharmacokinetics and biodistribution of lonidamine/paclitaxel loaded, EGFR-targeted nanoparticles in an orthotopic animal model of multi-drug resistant breast cancer. *Nanomedicine* 7(4):435–444
- Mitra S et al (2019) Impact of ROS generated by chemical, physical, and plasma techniques on cancer attenuation. *Cancers* 11(7):1030
- Mohammed E (2014) Qualitative and quantitative determination of folic acid in tablets by FTIR spectroscopy. *IJAPBC* 3:773–780
- Norton N et al (2020) Folate receptor alpha expression associates with improved disease-free survival in triple negative breast cancer patients. *NPJ Breast Cancer* 6(1):4
- Omid Z et al (2022) Status of breast cancer screening strategies and indicators in Iran: a scoping review. *J Res Med Sci* 27:21. [https://doi.org/10.4103/jrms.jrms\\_1390\\_20](https://doi.org/10.4103/jrms.jrms_1390_20)
- Pan Y et al (2020) Tumor-associated macrophages in tumor immunity. *Front Immunol*. <https://doi.org/10.3389/fimmu.2020.583084>
- Pandey MK et al (2016) Targeting cell survival proteins for cancer cell death. *Pharmaceuticals* 9(1):11
- Park C et al (2019) Induction of G2/M cell cycle arrest and apoptosis by genistein in human bladder cancer T24 cells through inhibition of the ROS-dependent PI3k/Akt signal transduction pathway. *Antioxidants* 8(9):327
- Piazzini V et al (2019) Nanostructured lipid carriers for oral delivery of silymarin: improving its absorption and in vivo efficacy in type 2 diabetes and metabolic syndrome model. *Int J Pharm* 572:118838
- Pineda MG et al (2014) Chitosan-coated magnetic nanoparticles prepared in one-step by precipitation in a high-aqueous phase content reverse microemulsion. *Molecules* 19(7):9273–9287
- Sadeghi-Aliabadi H et al (2013) Preparation and cytotoxic evaluation of magnetite (Fe<sub>3</sub>O<sub>4</sub>) nanoparticles on breast cancer cells and its combinatory effects with doxorubicin used in hyperthermia. *Avicenna J Med Biotechnol* 5(2):96
- Saha S et al (2016) Production of putrescine-capped stable silver nanoparticle: its characterization and antibacterial activity against multidrug-resistant bacterial strains. *Appl Nanosci* 6(8):1137–1147
- Sega EI, Low PS (2008) Tumor detection using folate receptor-targeted imaging agents. *Cancer Metastasis Rev* 27(4):655–664
- Silva VAJ et al (2013) Synthesis and characterization of Fe<sub>3</sub>O<sub>4</sub> nanoparticles coated with fucan polysaccharides. *J Magn Magn Mater* 343:138–143
- Singh S, Gupta AK (2011) Nitric oxide: role in tumour biology and iNOS/NO-based anticancer therapies. *Cancer Chemother Pharmacol* 67(6):1211–1224
- Stetefeld J, McKenna SA, Patel TR (2016) Dynamic light scattering: a practical guide and applications in biomedical sciences. *Biophys Rev* 8(4):409–427
- Strober W (2015) Trypan blue exclusion test of cell viability. *Curr Protoc Immunol*. <https://doi.org/10.1002/0471142735.ima03bs21>
- Sudo K (1995) Enzyme kinetics for enzyme immunoassay. *Nihon Rinsho* 53(9):2134–2139
- Suvarna V, Singh V, Murahari M (2019) Current overview on the clinical update of Bcl-2 anti-apoptotic inhibitors for cancer therapy. *Eur J Pharmacol* 862:172655
- Takeuchi Y, Nishikawa H (2016) Roles of regulatory T cells in cancer immunity. *Int Immunol* 28(8):401–409
- Taylor WR, Stark GR (2001) Regulation of the G2/M transition by p53. *Oncogene* 20(15):1803–1815
- Vuddanda PR et al (2014) Investigations on agglomeration and haemocompatibility of vitamin E TPGS surface modified berberine chloride nanoparticles. *BioMed Res Int*. <https://doi.org/10.1155/2014/951942>
- Wáng YXJ, Idée J-M (2017) A comprehensive literatures update of clinical researches of superparamagnetic resonance iron oxide nanoparticles for magnetic resonance imaging. *Quant Imaging Med Surg* 7(1):88
- Ying Y, Padanilam BJ (2016) Regulation of necrotic cell death: p53, PARP1 and cyclophilin D-overlapping pathways of regulated necrosis? *Cell Mol Life Sci* 73(11):2309–2324

- Zeinali M et al (2021) Prevention of UV-induced skin cancer in mice by gamma oryzanol-loaded nanoethosomes. *Life Sci* 283:119759
- Zhang B et al (2009) Receptor-mediated cellular uptake of folate-conjugated fluorescent nanodiamonds: a combined ensemble and single-particle study. *Small* 5(23):2716–2721
- Zhang Y et al (2013) ROS play a critical role in the differentiation of alternatively activated macrophages and the occurrence of tumor-associated macrophages. *Cell Res* 23(7):898–914
- Zhao R et al (2011) Mechanisms of membrane transport of folates into cells and across epithelia. *Annu Rev Nutr* 31:177–201
- Zhao R, Diop-Bove N, Goldman ID (2014) Enhanced receptor-mediated endocytosis and cytotoxicity of a folic acid-desacetylvinblastine monohydrazone conjugate in a pemetrexed-resistant cell line lacking folate-specific facilitative carriers but with increased folate receptor expression. *Mol Pharmacol* 85(2):310–321
- Kulkarni S, Sawadh P, Kokate K (2012) Synthesis and characterization of Fe<sub>3</sub>O<sub>4</sub> nanoparticles for engineering applications. In: International Conference on Benchmarks in Engineering Science and Technology (ICBEST).

### Publisher's Note

Springer Nature remains neutral with regard to jurisdictional claims in published maps and institutional affiliations.

**Ready to submit your research? Choose BMC and benefit from:**

- fast, convenient online submission
- thorough peer review by experienced researchers in your field
- rapid publication on acceptance
- support for research data, including large and complex data types
- gold Open Access which fosters wider collaboration and increased citations
- maximum visibility for your research: over 100M website views per year

**At BMC, research is always in progress.**

Learn more [biomedcentral.com/submissions](https://biomedcentral.com/submissions)

